우 수 논 문

[박 사 급]

연제: Rational function model-based image
matching for digital elevation model

연사: 박 정 환 (연세대학교)

RATIONAL FUNCTION MODEL-BASED IMAGE MATCHING FOR DIGITAL ELEVATION MODEL

CHOUNG-HWAN PARK (c142520@yonsei.ac.kr)

Yonsei University

Abstract

This paper presents a Rational Function Model (RFM)-based image matching technique for IKONOS satellite imagery. This algorithm adopts the object-space approach and reduces the search space within the confined line-shaped area called the Piecewise Matching Line (PML). Also, the detailed procedure of generating 3-D surface information using the Rational Function model Coefficients (RFCs) is introduced as an end-user point of view. As a result, the final generated Digital Elevation Model (DEM) using the proposed scheme shows a mean error of 2·2 m and RMSE of 3·8 m compared with that from 1:5000 digital map.

KEY WORDS: RFC, IMAGE MATCHING, PIECEWISE MATCHING LINE, DEM

INTRODUCTION

The new generation of high-resolution and multispectral IKONOS, launched in September 1999, and QuickBird imagery, launched in October 2001, have opened a new era in photogrammetry and remote sensing. The ground resolution of satellite imagery was remarkably improved and various users are now able to acquire more accurate 3-D terrain data. However, in order to keep the strategy that protects confidential information about the sensor, the developers directly involved in the high-resolution satellite project do not provide detailed orbital information about the sensor (in case of IKONOS). Though related data are provided, the accuracy level is considerably lower than the original (in case of QuickBird) (QuickBird Product Guide, 2003). For this reason, the concept of replacement sensor model, which enables general end-users to process the satellite imagery without knowing the physical sensor models, has been proposed (Greve, 1992; McGlone, 1996; OGC, 1999). Rational Function Model (RFM), one of the replacement sensor models, has been extensively used in IKONOS imagery. RFM defines the relation between the image space and object space in the form of polynomial ratios.

With no need to know the complicated algorithm, RFM can perform a series of photogrammetric processes such as 3-D positioning, Digital Elevation Model (DEM) generation, and ortho-rectification much faster than the conventional method. After RFM has been verified as a replacement sensor model (Madani, 1999; Dowman and Dolloff, 2000; Tao et al., 2000), several researchers assessed the accuracy

of 3-D positioning using RFM (Yang, 2000; Grodecki and Dial, 2001; Tao and Hu, 2001(a)~(c); Sohn et al., 2004; Noguchi et al., 2004). Furthermore, a comparison of the accuracy between two reconstruction algorithms, inverse RFM and forward RFM, was carried out (Tao and Hu, 2002).

The above mentioned studies proved that RFM could satisfy several important standards of the replacement sensor model such as general tools for mapping, accurate 3-D positioning, and real time processing. However, RFM has a shortcoming in that the accuracy of generated 3-D terrain data definitively depends on the accuracy of Rational Function model Coefficients (RFCs) supplied by the vendors. In other words, if the accuracy of RFCs is much worse than the original pixel resolution, the generated product can not be better than pixel accuracy. Therefore, in order to acquire high quality product, a methodology for determining the precise RFCs or refining the supplied RFCs is required and a solution for DEM generation using the RFCs has to be developed. However, there have only been a few detailed publications about DEM generation using RFM. Especially, it is difficult to find studies related to image matching using RFM, even though it is a critical step in generating DEM.

The first attempt to refine the RFCs was done by Hu and Tao (2002). In their study, they suggested two refinement methods, Batch Iterative Least Squares (BILS) and Incremental Discrete Kalman Filtering (IDKF) with additional Ground Control Points (GCPs). They described that the accuracy of RFM solutions could be improved when a significant number of new GCPs was available. Fraser and Hanley (2003) proposed a new method which could improve the accuracy of 3-D positioning and generate bias corrected RFCs through removal of exterior orientation biases in RFCs. Also, Grodecki and Dial (2003) described block adjustment algorithm for high-resolution satellite imagery using bias compensation method proposed by Fraser and Hanley. However, even if accurate RFCs are obtained from the refinement methods, it is not possible to acquire the high quality 3-D terrain data without a successful matching strategy.

Image matching for satellite imagery is not an easy work especially when the geometric differences between the stereo satellite images are quite large. The epipolar solution, which is popular in aerial photograph, has some difficulties to be applied to satellite imagery due to different geometric characteristics (Otto, 1988; Baltsavias, 1993; Kim, 2000). Accordingly, an alternative algorithm using the geometric model between image space and object space was developed (Baltsavias, 1993). This method provided a clue for matching solution of satellite imagery. For SPOT stereo imagery, it was reported that the accuracy of generated DEM using the proposed algorithm is in the 10 m range. However, this technique needs a physical sensor model and ephemeris data about the sensor that the current high-resolution satellite imagery does not provide to the general users. Recently, using IKONOS imagery, Jacobsen tested image-based region growing matching for Digital Surface Models (DSM) generation over the urban area (Jacobsen, 2001; Jacobsen, 2002). His method needs the pixel positions of manually measured control and tie points as a start value.

This paper offers the advanced matching solution to resolve the inherent problems for the high-resolution satellites that adopt RFM as a basic sensor model. To update the vendor-provided RFCs for image matching, the scheme of Fraser and Hanley's (2003) was applied and evaluated. The proposed matching algorithm reduces the search space using object-space constraints and provides an initial position for image matching. In the following sections, the detailed process for RFM-based image matching is described. The procedure for DEM generation using the RFCs as an end-user point of view is also introduced. In order to verify the applicability for high-resolution satellite imagery and check the performance of proposed matching scheme, IKONOS stereo pairs with RFCs are tested. Finally, the absolute accuracy of generated DEM over the test site is presented.

REFINEMENT OF RFM SOLUTION USING BIAS COMPENSATION

General Description of RFM

RFM can be divided into two scenarios, terrain-independent and terrain-dependent, depending on whether the physical sensor model is known or unknown. RFM is further divided into forward RFM and inverse RFM according to the relationship between object space and image space (Yang, 2000; Tao and Hu, 2001(b)). In the case of forward RFM, the ratios of polynomials of object space coordinates define the image space coordinates. To minimize the errors during the matrix computation, both image space coordinates and object space coordinates are normalized in the range of -1.0 to +1.0 by applying offsetting and scaling factors (OGC, 1999; Tao et al., 2000). General forms of forward RFM can be written as Equation 1:

$$r = \frac{p_1(\varphi, \lambda, h)}{p_2(\varphi, \lambda, h)}, \quad c = \frac{p_3(\varphi, \lambda, h)}{p_4(\varphi, \lambda, h)} \tag{1}$$

where r and c are the normalized row and column indices of pixels in the image space and φ, λ, and h are the normalized coordinates in the object space. In Equation 1, polynomials p_i have the general form as described in Equation 2:

$$p_i(\varphi, \lambda, h) = \sum_{i=0}^{m_1} \sum_{j=0}^{m_2} \sum_{k=0}^{m_3} a_{ijk} \varphi^i \lambda^j h^k \tag{2}$$

where a_{ijk} are polynomial coefficients, called RFCs, and m_1, m_2, and m_3 are the available maximum powers of polynomial typically limited to 3.

Equation 1 shows the transformation from object space to image space. On the other hand, when converting from image space to object space, Equation 3, which is called inverse RFM, is used (Yang, 2000):

$$\varphi = \frac{p_5(r,c,h)}{p_6(r,c,h)}, \quad \lambda = \frac{p_7(r,c,h)}{p_8(r,c,h)} \tag{3}$$

Equation 3 mainly expresses the horizontal object space coordinates as rational functions of image space coordinates and the elevation of object space coordinates.

Bias Corrected RFM Solution

Out of the two models, the forward RFM generally shows better fitting and reconstruction result (Tao and Hu, 2002). In fact, the RFCs supplied by the IKONOS satellite use the forms shown in Equations 4 and 5 based on the forward RFM.

$$
\begin{aligned}
p_1 (or \; p_3) = {} & a_1 + a_2\lambda + a_3\varphi + a_4 h + a_5\lambda\varphi + a_6\lambda h + a_7\varphi h + a_8\lambda^2 \\
& + a_9\varphi^2 + a_{10}h^2 + a_{11}\varphi\lambda h + a_{12}\lambda^3 + a_{13}\lambda\varphi^2 + a_{14}\lambda h^2 \\
& + a_{15}\lambda^2\varphi + a_{16}\varphi^3 + a_{17}\varphi h^2 + a_{18}\lambda^2 h + a_{19}\varphi^2 h + a_{20}h^3
\end{aligned}
\tag{4}
$$

$$
\begin{aligned}
p_2 (or \; p_4) = {} & 1 + b_1\lambda + b_2\varphi + b_3 h + b_4\lambda\varphi + b_5\lambda h + b_6\varphi h + b_7\lambda^2 \\
& + b_8\varphi^2 + b_9 h^2 + b_{10}\varphi\lambda h + b_{11}\lambda^3 + b_{12}\lambda\varphi^2 + b_{13}\lambda h^2 \\
& + b_{14}\lambda^2\varphi + b_{15}\varphi^3 + b_{16}\varphi h^2 + b_{17}\lambda^2 h + b_{18}\varphi^2 h + b_{19}h^3
\end{aligned}
\tag{5}
$$

In these equations, φ is normalized geodetic latitude, λ is normalized geodetic longitude, and h is the normalized height above the WGS-84 ellipsoid.

In the case of high-resolution satellite imagery that does not offer the precise orbital information, it is an alternative to refine the given RFCs in order to acquire the detailed 3-D terrain data. Hu and Tao (2002) proposed two refinement methods, BILS and IDKF, for the RFCs. The former adopts a simple algorithm, but good results can be expected only under conditions where the covariance matrices for the RFCs and the image measurements are available (supplied by the data vendor that calculated the RFM initially). Also, a large number of GCPs is used. The latter can be refined with only a few numbers of GCPs, but requires a relatively complex procedure.

Fraser and Hanley (2003) provided more practical method. This method incorporates a correction directly into the original RFCs in order to produce bias-free object point coordinates, nominally to meter-level absolute accuracy. It can overcome the limits of BILS and solve the complication of IDKF. Grodecki and Dial (2003) presented the RFC block adjustment model using the exterior orientation bias

compensation for IKONOS imagery proposed by Fraser and Hanley. It is reported that the RFC block adjustment model for the IKONOS satellite imagery is as accurate as the IKONOS ground station block adjustment with the physical camera model.

We also adopted the scheme of Fraser and Hanley's to refine the RFCs and improved the efficiency of the proposed matching method in this study. The refinement model can be written as Equation 6 and Equation 7:

$$R_i = \Delta R_i + [r_i(\varphi, \lambda, h) \cdot row_s + row_o] + \upsilon_{R_i} \tag{6}$$

$$C_i = \Delta C_i + [c_i(\varphi, \lambda, h) \cdot column_s + column_o] + \upsilon_{C_i} \tag{7}$$

where, R_i and C_i are observed original row and column coordinates of the i th GCP, ΔR_i and ΔC_i are refinement functions, $r_i(\varphi, \lambda, h)$ and $c_i(\varphi, \lambda, h)$ are the calculated normalization coordinates of i th GCP, row_s and $column_s$ are the scale values of image space (supplied by Space Imaging, Inc.), row_o and $column_o$ are the offset values of image space (supplied by Space Imaging, Inc.), υ_{R_i} and υ_{C_i} are random errors.

The refinement functions in the image space generally can be divided into four cases (Grodecki and Dial, 2003).

$$\Delta R = \alpha_1, \quad \Delta C = \beta_1 \tag{8}$$

$$\Delta R = \alpha_1 + \alpha_2 \cdot R, \quad \Delta C = \beta_1 + \beta_2 \cdot R \tag{9}$$

$$\Delta R = \alpha_1 + \alpha_2 \cdot C, \quad \Delta C = \beta_1 + \beta_2 \cdot C \tag{10}$$

$$\Delta R = \alpha_1 + \alpha_2 \cdot C + \alpha_3 \cdot R, \quad \Delta C = \beta_1 + \beta_2 \cdot C + \beta_3 \cdot R \tag{11}$$

In these equations, $\alpha_1, \alpha_2, \alpha_3, \beta_1, \beta_2, \beta_3$ are image adjustment parameters for bias compensation.

As discussed in Grodecki and Dial's result, for images shorter than 50 km, Equation 8 is enough to compensate the biases because all refinement models show almost same accuracy.

After bias compensation process, bias corrected RFCs can be acquired with incorporating bias compensation into the originally supplied RFCs. The bias corrected RFCs for imagery is produced as Equation 12 and Equation 13.

$$r + \Delta r = \frac{p_1(\varphi, \lambda, h)}{p_2(\varphi, \lambda, h)}, \quad \Delta r = \Delta R / row_s \tag{12-1}$$

$$c + \Delta c = \frac{p_3(\varphi, \lambda, h)}{p_4(\varphi, \lambda, h)}, \quad \Delta c = \Delta C / column_s \tag{12-2}$$

$$r = \frac{(a_1 - \Delta r) + \cdots (a_{20} - b_{19}\Delta r)h^3}{1 + b_1\lambda + b_2\varphi + \cdots b_{19}h^3}, \quad c = \frac{(c_1 - \Delta c) + \cdots (c_{20} - d_{19}\Delta c)h^3}{1 + d_1\lambda + d_2\varphi + \cdots d_{19}h^3} \tag{13}$$

All numerator terms of original RFCs in Equation 1 are modified by including bias compensation. This algorithm enables users to facilitate bias-free 3-D positioning and 3-D surface reconstruction efficiently.

RFM-BASED IMAGE MATCHING USING PIECEWISE MATCHING LINE

Problems in conventional image matching for satellite imagery

The object-space approach, which uses the geometry between image space and object space, is a useful means of image matching in terms of efficiency and quickness (Zhang, 1991). If radiometric and geometric differences exist in the stereo images, the conventional image-based matching may show high probability of mismatching. It also adopts an isolated algorithm that searches the conjugate points within the template. Therefore, the matching confidence seriously decreases under conditions where the monotonous image has a low texture or the texture patterns in the image are repetitive (Lo and Mulder, 1992). The frequently recommended solution for this circumstance is the epipolar constraint.

The epipolar constraint is very helpful in solving correspondence problems in image matching. Many of the existing stereo matching algorithms use this constraint to confine search dimensions, reduce processing time, and achieve reliable match estimates (Zhang et al., 1995; Kim, 2000). However, the epipolar geometry in the case of satellite imagery is defined as a curve, not as a line, and unlike aerial photographs, it contains complex characteristics. Also, since most of the recent high-resolution satellites provide the replacement sensor model with relatively lower accuracy than the original resolution, it is not valid to acquire the high quality 3-D terrain data even if it is possible to make the epipolar image. An alternative matching solution for the satellite imagery is to limit the search space using satellite geometry and object-space information.

In this study, the advanced matching algorithm with the following characteristics is proposed. First, our method is an expanded object-space based approach. Second, it is an appropriate algorithm for high-resolution satellite imagery which adopts RFM as a basic sensor model. Figure 1 compares the concept of conventional image-based matching and RFM-based image matching using object-space constraints. In Figure 1, Piecewise Matching Line (PML) serves as a matching route which connects point P_1 with point P_1', the conjugate point of P_1. The PML limits the possible re-projected area on the right image using the object space information. Therefore, image matching is performed within the part which has the

high potential as a conjugate point. The detailed processes for creating the PML are explained in the following section.
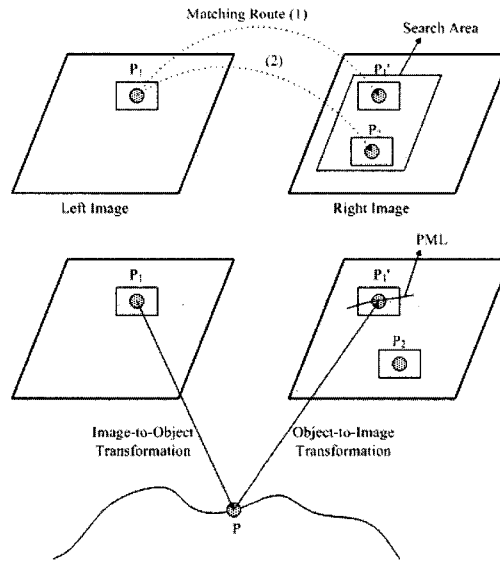

Fig. 1. Conventional image-based matching vs. the proposed RFM-based image matching.

RFM-Based Image Matching Algorithm

In satellite imagery, due to off-nadir effects, pixels may be larger than the nominal resolution and geometric distortion may occur depending on the look- angle. These factors clearly show the limitations of conventional image-based matching. Therefore, an alternative approach is required to solve matching problems for high-resolution satellite imagery. Figure 2 depicts the flowchart of the proposed matching scheme.
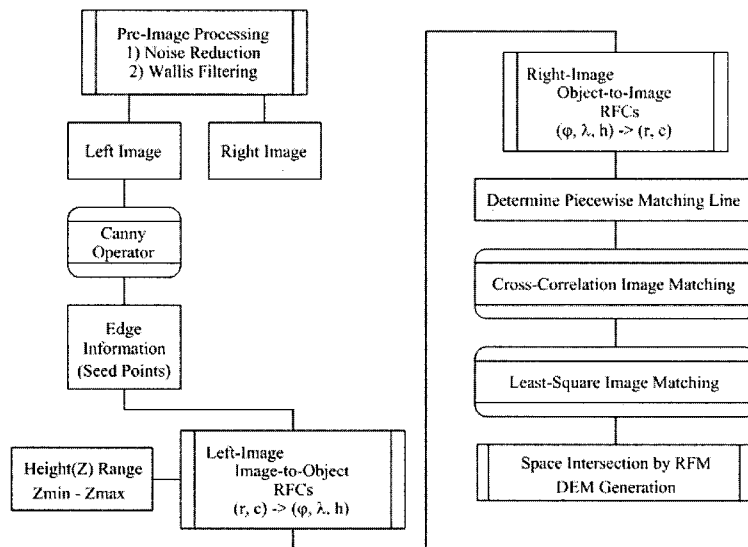

Fig. 2. Flowchart of RFM-based image matching algorithm.

The first step is to extract seed points for image matching. The Canny edge detector is applied to the left image. The Canny operator is probably the most widely used edge detector. The goals of the Canny operator are stated explicitly (Canny, 1986).

(a) Good Detection: the ability to locate and mark all real edges.

(b) Good Localization: minimal distance between the detected edge and real edge.

(c) Clear Response: only one response per edge.

The seed points extracted from the left image are re-projected to the right image through a two-step process, and the search space for image matching is restricted within the elevation range of object space. The following describes the image-to-object and the object-to-image transformation using forward RFM.

• Image-to-Object Transformation

The geometry of image space and object space can be expressed through two forms of RFM, forward and inverse. Equation 3 (inverse form) shows the direct transformation from image to object space. Equation 1 (forward form) represents a more general type of RFM (the form provided by Space Imaging, Inc.) and shows an improved accuracy than the inverse (Tao and Hu, 2002). In this study, forward RFM is selected to define transformation from image to object space and vice versa.

If the RFCs are supplied for the stereo images and the conjugate points on image are known, the corresponding object point can be uniquely defined. However, if only one image point is known, the object point does not have a unique solution. In other words, in order to set up the image-to-object transformation using one image point, one unknown variable must be eliminated. Assuming that the elevation is a known value, an approximate transformation from image space to object space can be constructed. The assumed elevation range can be divided into several levels. For each elevation level, two error equations, such as Equation 14, are obtained.

$$f(r)_{ref} = \frac{p_1(\varphi,\lambda,h_i)}{p_2(\varphi,\lambda,h_i)} - r_{ref}, \quad f(c)_{ref} = \frac{p_3(\varphi,\lambda,h_i)}{p_4(\varphi,\lambda,h_i)} - c_{ref} \tag{14}$$

where h_i refers to the normalized elevation value of target area. If the elevation information is not available, it can be assumed using the scale and offset values of object space provided with the imagery.

Equation 14 can be written as a matrix form as shown in Equation 15, and the stereo images are normalized separately using different offset and scale values for object coordinates. Therefore, the normalization parameters should be introduced so that the object coordinates are used in adjusting Equation 15. The object coordinates at various elevation levels are calculated using the least squares solution.

$$\begin{bmatrix} v_{r_{ref}} \\ v_{c_{ref}} \end{bmatrix} = \begin{bmatrix} \dfrac{\partial f(r)_{ref}}{\partial \varphi} \dfrac{1}{\varphi_s} & \dfrac{\partial f(r)_{ref}}{\partial \lambda} \dfrac{1}{\lambda_s} \\ \dfrac{\partial f(c)_{ref}}{\partial \varphi} \dfrac{1}{\varphi_s} & \dfrac{\partial f(c)_{ref}}{\partial \lambda} \dfrac{1}{\lambda_s} \end{bmatrix} \begin{bmatrix} \Delta \varphi_G \\ \Delta \lambda_G \end{bmatrix} - \begin{bmatrix} r_{ref} - \hat{r}_{ref} \\ c_{ref} - \hat{c}_{ref} \end{bmatrix} \cdot \tag{15}$$

where

$$\frac{\partial f(r)_{ref}}{\partial \varphi} = \frac{\partial p_1(\varphi,\lambda,h_i)/\partial \varphi \cdot p_2(\varphi,\lambda,h_i) - p_1(\varphi,\lambda,h_i) \cdot \partial p_2(\varphi,\lambda,h_i)/\partial \varphi}{p_2(\varphi,\lambda,h_i) \cdot p_2(\varphi,\lambda,h_i)}$$

$$\frac{\partial f(c)_{ref}}{\partial \varphi} = \frac{\partial p_3(\varphi,\lambda,h_i)/\partial \varphi \cdot p_4(\varphi,\lambda,h_i) - p_3(\varphi,\lambda,h_i) \cdot \partial p_4(\varphi,\lambda,h_i)/\partial \varphi}{p_4(\varphi,\lambda,h_i) \cdot p_4(\varphi,\lambda,h_i)}$$

and the remaining partial derivatives are similarly calculated. $\Delta \varphi_G$ and $\Delta \lambda_G$ indicate the corrections of object coordinates. $\hat{r}_{ref}$ and $\hat{c}_{ref}$ are the estimated value by substituting initial values into Equation 1 after normalization. φ_s and λ_s are the scale values of object space in the left image.

To obtain the initial values $(\varphi_G^0, \lambda_G^0)$ for object coordinates, the first-order RFM is used as shown in Equation 16.

$$r_{ref} = \frac{a'_1 + a'_2 \lambda_G^0 + a'_3 \varphi_G^0 + a'_4 h_{G_i}}{b'_1 + b'_2 \lambda_G^0 + b'_3 \varphi_G^0 + b'_4 h_{G_i}} \qquad c_{ref} = \frac{c'_1 + c'_2 \lambda_G^0 + c'_3 \varphi_G^0 + c'_4 h_{G_i}}{d'_1 + d'_2 \lambda_G^0 + d'_3 \varphi_G^0 + d'_4 h_{G_i}} \tag{16}$$

where

$$a'_1 = a_1 \varphi_s \lambda_s h_s - a_2 \varphi_s \lambda_o h_s - a_3 \varphi_o \lambda_s h_s - a_4 \varphi_s \lambda_s h_o, \ a'_2 = a_2 \varphi_s h_s, \ a'_3 = a_3 \lambda_s h_s, \ a'_4 = a_4 \varphi_s \lambda_s$$

and the remaining terms are similarly calculated. $\varphi_s, \lambda_s, h_s, \varphi_o, \lambda_o, h_o$ are the scale and offset values of object space in the left image. h_{G_i} is the assumed elevation value of object space.

Equation 16 can be written into a matrix form as shown in Equation 17.

$$\begin{bmatrix} a'_2 - b'_2 r_{ref} & a'_3 - b'_3 r_{ref} \\ c'_2 - d'_2 c_{ref} & c'_3 - d'_3 c_{ref} \end{bmatrix} \begin{bmatrix} \lambda_G^0 \\ \varphi_G^0 \end{bmatrix} = \begin{bmatrix} -(a'_1 - b'_1 r_{ref}) - (a'_4 - b'_4 r_{ref}) h_{G_i} \\ -(c'_1 - d'_1 c_{ref}) - (c'_4 - d'_4 r_{ref}) h_{G_i} \end{bmatrix} \tag{17}$$

Finally, the updated 3-D object coordinates are obtained as follows.

$$\varphi_G = \varphi_G^0 + \Delta \varphi_G, \qquad \lambda_G = \lambda_G^0 + \Delta \lambda_G, \qquad h_G = h_{G_i} \tag{18}$$

▪ Object-to-Image Transformation

The 3-D object coordinates calculated in the previous section can be easily re-projected to the right image by the RFCs of right image. This process is important in that the search space for image matching

is limited to linear-shape area. The re-projected image coordinates in all elevation levels construct the PML. Actual image matching is performed along the PML. The proposed scheme makes it simpler and faster to perform image matching than the hyperbolic epipolar solution for satellite imagery. Figure 3 illustrates the PML on the right image at each elevation level (point P_R is a potential conjugate point of point P_L).
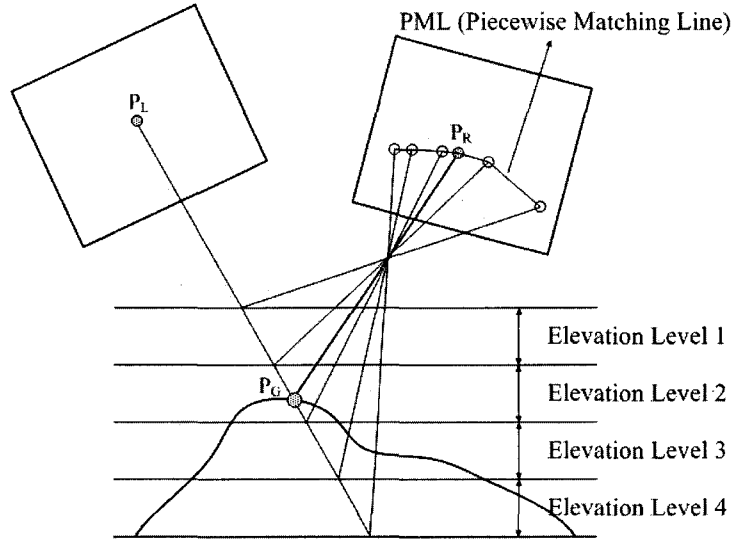

Fig. 3. Piecewise Matching Line according to each elevation level.

To determine the PML, the linear equations (Equation 19) in each elevation level are used:

$$R_i = \frac{R_{high} - R_{low}}{C_{high} - C_{low}}(C_i - C_{high}) + R_{high}$$ (19)

where R_{high} and C_{high} are the image coordinates corresponding to the highest elevation in each level and R_{low} and C_{low} are the image coordinates corresponding to the lowest elevation in each level

Once the initial position for image matching is defined along the PML, the template matching by means of cross-correlation is first performed and the least squares matching for the sub-pixel accuracy is again applied.

EXPERIMENTAL RESULTS AND ANALYSIS

Data Sets

To test two experiments, refinement of the RFCs and RFM-based image matching, IKONOS stereo images (Geo level) were used taken in November 22, 2001. The stereo pairs cover the Daejeon Metropolitan City and its surroundings, located in the middle of South Korea. The test site, shown in

Figure 4, was selected for DEM generation using the proposed matching scheme. It has an area of about 1.5km×1.5km.

Fig. 4. Test site (1340 column × 1548 row).

Experiment-I: Refinement of the RFCs

Space Imaging, Inc., which is the vendor of IKONOS satellite imagery, does not supply satellite orbital information. Instead, it allows end-users to utilize the RFCs in satellite image processing. The specified horizontal accuracy of standard IKONOS Geo products is 25 m CE90 (Grodecki and Dial, 2001). The RFCs of IKONOS imagery contain a total of 78 polynomial coefficients for each image (the actual number of polynomial coefficients is 59 since the denominator terms for the line and column is equal). The reference coordinate system adopts the geodetic coordinates on WGS-84 ellipsoid.

For the refinement of RFCs, 35 GCPs are collected using the precise DGPS technique. Since GPS adopts the WGS-84 ellipsoid, which is the same system as IKONOS, additional conversion is not needed. Because the accuracy level of the original RFCs is not suitable for RFM-based image matching, two refinement functions, Equation 8 and Equation 11, are applied to compensate bias in RFCs. Figure 5 shows plots of bias vectors in stereo images. The bias vectors show the differences between previously observed image coordinates and RFC-based image coordinates.

In Figure 5, the direction and magnitude of biases in left and right images show a different pattern. Especially, the biases in the row of right image show RMSE of about 16·5 pixel. Our test conditions do not correspond with the test-bed data, which showed the systematic bias pattern in Fraser and Hanley's (2003) case. Their test is performed with precise GCPs and image coordinate data, multiple GPS and image measurements are done for each GCP by computing a best-fitting ellipse to six or more edge points around the circumference of the feature, in both object and image space. When end-users compensate biases of their data sets, the situation such as Figure 5 is often happened than the case which has systematic errors. Also, it is difficult for general end-users to prepare accurate GCP data for their test sites

since it is costly and time-consuming task. Therefore, in order to verify the practical application of bias compensation technique, the experiment for the general data type which has a non-systematic error patterns is required.
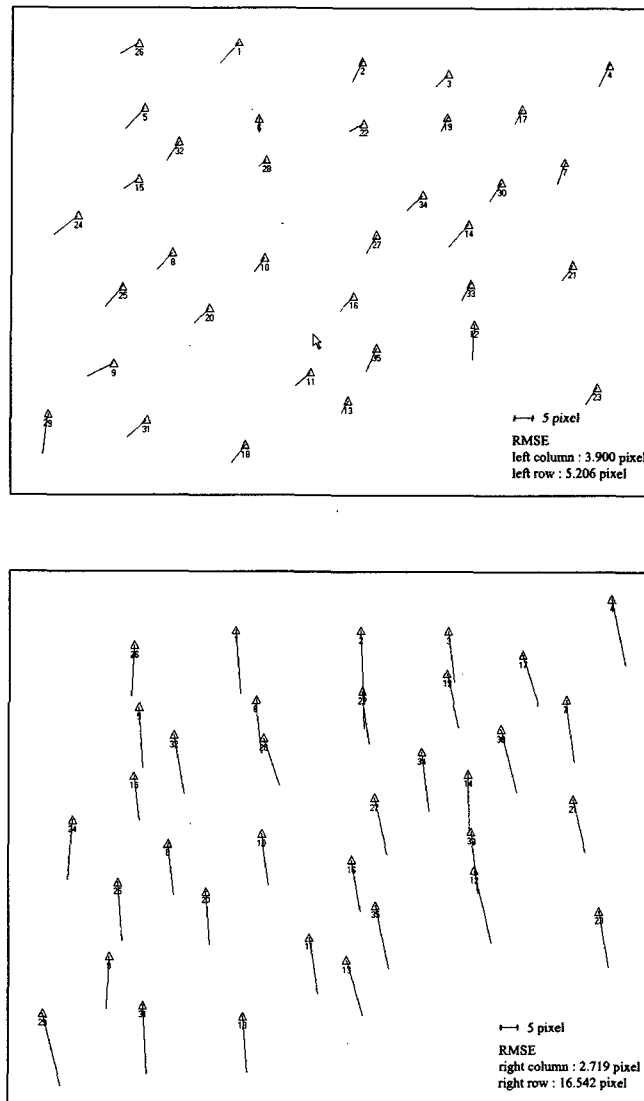

Fig. 5. Image coordinate biases in IKONOS stereo images (a) left and (b) right.

Five cases of GCP configurations (1, 2, 4, 6, and 10 points) are tested for two refinement functions and the accuracy of bias compensation is checked. Table I provides summaries of results obtained in the RFC bias compensation using the models of both Equation 8 and Equation 11. For two models, Table I shows that no big differences exist in terms of accuracy. This outcome indicates that a single offset term is sufficient for bias compensation in stereo images. It corresponds with results of Grodecki and Dial (2003) and those of Fraser and Hanley (2003). Although the accuracy is relatively lower than the previous two studies, the effect after bias compensation is satisfiable in comparison with before bias compensation.

Table I. Accuracy of bias compensation in IKONOS stereo images (RMSE, unit: pixel)

Model	Equation 8				Equation 11			
GCP	left		right		left		right	
Config.	column	row	column	row	column	row	column	row
1	1.646	3.310	1.616	3.066	1.654	3.334	1.616	3.066
2	1.714	2.603	1.771	3.022	1.639	2.967	1.630	3.066
4	1.734	2.480	1.823	3.235	1.576	2.275	1.682	3.190
6	1.666	2.187	1.529	2.920	1.643	2.461	1.638	3.174
10	1.704	2.139	1.532	3.024	1.682	2.099	1.547	3.033

Actually, for left image, RMSE without GCP are 3·9 pixel in column and 5·2 pixel in row. The addition of one GCP reduce to 1·6 pixel and 3·3 pixel, respectively. For right image, RMSE of 2·7 pixel in column and 16·5 pixel in row reduce to 1·6 pixel and 3·1 pixel. Therefore, this experiment confirms refinement algorithm using bias compensation to be effective method for general end-users.

Experiment-II: RFM-Based Image Matching Using Bias Corrected RFCs

IKONOS stereo images are supplied with the RFCs calculated from Space Imaging, Inc. However, the supplied RFCs are not suitable for acquiring the detailed 3-D terrain data. Therefore, bias corrected RFCs are used to test our matching algorithm. In order to determine the initial position for image matching, the PML is first derived from a priori (or assumed) object-space information and two-step transformations. The elevation range (50 ~ 160 m) of test site is divided into 11 levels each with 10 m intervals. To check the accuracy of PML, total five conjugate points are manually selected as shown in Figure 6 (f). Figure 6 (a) to (e) show the generated PMLs using original RFCs and bias corrected RFCs, and display the distance between the conjugate point and the two PMLs.

The PMLs over the other parts of imagery display similar patterns as shown in Figure 6 (a) to (e) (we actually generate PML from nine areas in entire image and analyze their accuracy). In case the newly generated PML using the bias corrected RFCs, the maximum distance between the PML and the conjugate point shows about 1.3 pixels. As a result, it is confirmed that the PML can be substituted for complex epipolar curve in satellite imagery. The presented matching scheme in this study may work well for the high resolution satellite imagery which adopts RFM as a basic sensor model. To guarantee more stable matching performance, the additional search space in practical experiment is extended to ± 2 pixels around the PML.
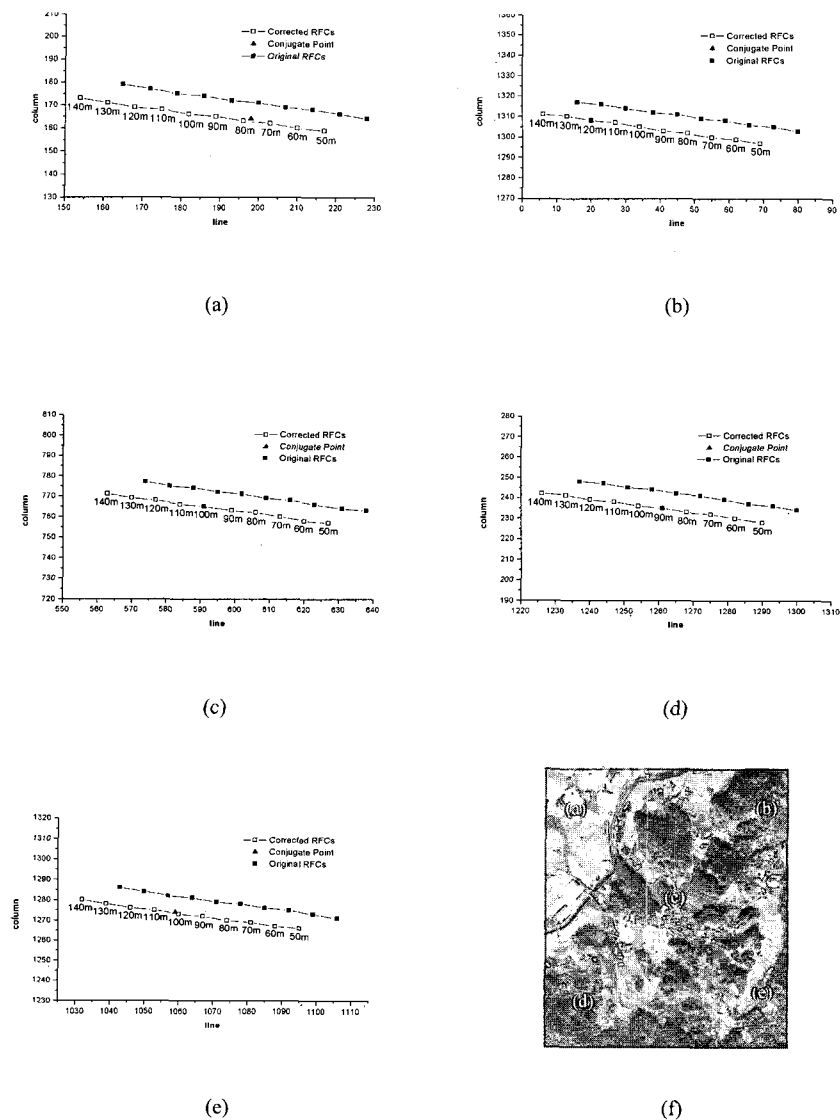
Fig. 6. The generated Piecewise Matching Line using original RFCs and bias corrected RFCs.

Before the image matching process, a two-step pre-processing is applied for the original images. First, the periodic and pattern noise is eliminated. Second, the Wallis filter, which is an adaptive nonlinear local contrast enhancement filter, is applied for effective extraction of the seed points. From the left image, a total of 149084 seed points are extracted using the Canny edge detector. RFM-based image matching is then performed along the PML. For each elevation level, least squares matching is again applied to ensure the sub-pixel accuracy. Also, the conventional image-based matching is performed under the same area and same condition. The final RFM-based matching results for each elevation level are summarized in Table II. In Table II, MPs refers to the number of matched points. RMP means the ratio of matched points, which can be written as (the number of MPs)/(the number of seed points).

Table II. Final matching results using RFM-based image matching in IKONOS stereo images

(MPs: Matched points, RMP: Ratio of the MPs)

Seed points	149084	
Elevation level (unit: m)	MPs	RMP
1 (50 ~ 60)	1324	0·008
2 (60 ~ 70)	4116	0·027
3 (70 ~ 80)	18966	0·127
4 (80 ~ 90)	31624	0·212
5 (90 ~ 100)	20614	0·138
6 (100 ~ 110)	15727	0·105
7 (110 ~ 120)	12682	0·085
8 (120 ~ 130)	5886	0·039
9 (130 ~ 140)	5356	0·035
10 (140 ~ 150)	4629	0·031
11 (150 ~ 160)	3546	0·023

Generally, a large number of seed points are matched in level 3 to level 7 where 60% of actual elevation data are distributed. The result matches well with the elevation histogram of reference DEM shown in Figure 7. Also, total MP in this elevation ranges reaches about 124470 conjugate points. On the contrary, the image-based matching shows only 44254 conjugate points and consumes more matching times. The proposed RFM-based matching algorithm using the PML proves to be more accurate, more efficient, and faster than the conventional image-based matching which uses only pixel value in image space.
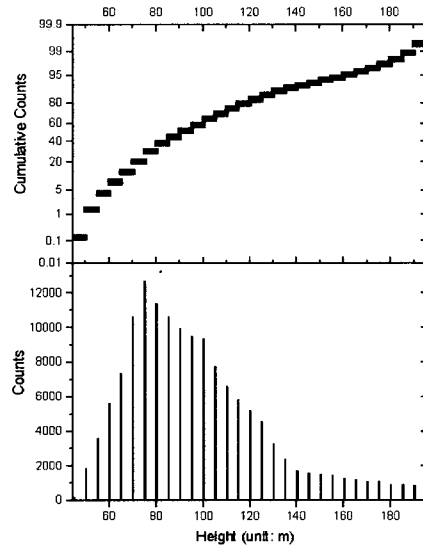
Fig. 7. The elevation histogram of reference DEM.

In the first matching experiment, the elevation range of object space is assumed using the prior information. However, it is often happened that the elevation information of object space is not available. End-users in this case have no choice but to assume elevation range using the provided scale and offset value of object space. Generally, the derived elevation range has too large scale and can be exaggerated than those of the actual terrain. Accordingly, we inspect the matching performance in the case of the expanded elevations. Table III summarizes the matching results assuming the test site has a higher elevation than those of the actual terrain. In Table III, when the assumed range is not fit to the elevation of actual terrain, the matching results are suddenly deteriorated. Therefore, the proposed RFM-based matching scheme using the PML proves to be the suitable and efficient model in matching application.

Table III. Matching results in the higher elevations than the actual terrain (MPs: Matched points)

Seed points	149084
Elevation level (unit: m)	MPs
1 (200 ~ 210)	159
2 (210 ~ 220)	170
3 (220 ~ 230)	163
4 (230 ~ 240)	108
5 (240 ~ 250)	107

All final matched points (Table II) are transformed to 3-D object coordinates through the space intersection using forward RFM. The DEM over the test site is generated using the Kriging interpolation and has a grid spacing of 5m. Figure 8 shows the final DEM over the test site. For the evaluation of vertical absolute accuracy, the reference DEM over the same area is interpolated from 1:5000 digital map contours and additional break lines. The vertical accuracy of reference DEM is specified as 1m RMSE (NGIS Product Specification, 2002). The maximum error of contours is allowed within 2m.
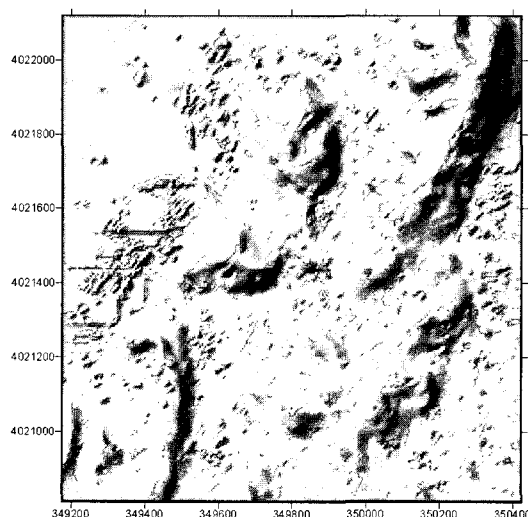

Fig. 8. The generated DEM using RFM-based image matching with bias corrected RFCs.

The vertical differences between the two DEMs are calculated and statistics are summarized in Table IV. For the absolute accuracy, Table IV shows a mean error of 2·2 m, RMSE of 3·8 m. The result is similar to that of Tao and Hu (2002), in which the vertical differences between the DEM from the Canadian Digital Elevation Data (CDED) and the 3-D reconstruction data using the RFM were checked, and the result shows a mean error of 3·8 m, RMSE of 4·2 m. The result of this study can also be compared with that of Zhang (2002), in which the vertical distances between the generated DSM from IKONOS stereo images and the DSM from the digital map of 1:5000 were calculated, and the result shows a mean error of 1·4 m, RMSE of 3·9 m.

Table IV. Absolute accuracy of the generated DEM (unit: meter)

Source	Height		
	RMSE	Mean Error	Max. Error
Digital Map	3·831	2·230	21.325

CONCLUSIONS

Most high-resolution satellite products supply an accuracy that is relatively low and inconsistent with their original image quality. Though the precision products are available, they are not only prohibited in some countries but are also expensive. Therefore, in order to acquire high quality outcomes, an accurate sensor parameter and a stable matching strategy is essential. In this study, a refinement solution using bias compensation is used to acquire accurate sensor parameter. For a stable matching performance, the RFM-based image matching algorithm using the PML is presented.

In the first experiment, the bias corrected RFCs are derived from method developed by Fraser and Hanley since the original RFCs of IKONOS imagery are not suitable for producing the detailed 3-D terrain information. Before bias compensation, RMSE of left imagery are 3·9 pixel in column and 5·2 pixel in row, and RMSE of right imagery are 2·7 pixel in column and 16·5 pixel in row. After bias compensation, the addition of one GCP reduce to 1·6 pixel and 3·3 pixel, 1·6 pixel and 3·1 pixel, respectively. This result confirms that refinement of the RFCs using bias compensation is efficient solution for GCP data even the biases do not show systematic pattern.

In the second experiment, RFM-based image matching is applied for IKONOS stereo images. The object-space constraints, or the elevation range, are introduced to reduce the search space for image matching and the bias corrected RFCs are used to generate PMLs. This approach leads the distance between the PML and the actual conjugate point to within 1.3 pixels. Also, total RMP in all elevation levels, which are equivalent to the elevation ranges of real terrain, is about 83%. As a result, the proposed matching scheme is useful for high-resolution satellite imagery when the epipolar solution is not practicable or difficult to apply. The absolute accuracy of generated DEM shows RMSE of 3·8 m in IKONOS.

This paper shows the possibility of precise surface reconstruction using IKONOS stereo images. The proposed RFM-based image matching facilitates the DEM generation using high-resolution satellite imagery which adopts RFM as the basic sensor model and is superior to the conventional algorithm considering the accuracy and real-time processing of RFM.

REFERENCES

BALTSAVIAS, E. P. and STALLMANN, D., 1993. SPOT stereo matching for digital terrain model generation. *Proceedings of 2nd swiss Symposium on Pattern Recognition and Computer Vision*, Zurich. 61-72.

CANNY, J., 1986. A computational approach to edge detection. *IEEE Transactions on Pattern Analysis and Machine Intelligence*, 8(6): 679-698.

DOWMAN, I. and DOLLOFF, J. T., 2000. An evaluation of rational functions for photogrammetric restitution. *International Archives of Photogrammetry and Remote Sensing*, 33(B3): 254-266.

FRASER, C. S. and HANLEY, H. B., 2003. Bias compensation in rational functions for IKONOS satellite imagery. *Photogrammetric Engineering & Remote Sensing*, 69(1): 53-57.

GREVE, C. W., MOLANDER, C. W. and GORDON D. K., 1992. Image processing on open systems. *Photogrammetric Engineering & Remote Sensing*, 58(1): 85-89.

GRODECKI, J. and DIAL, G., 2001. IKONOS geometric accuracy. *Joint Workshop of ISPRS Working group I/2, I/5 and IV/7 on High Resolution Mapping from space 2001*, Hannover. CD-ROM. 10 pages

GRODECKI, J. and DIAL, G., 2003. Block adjustment of high-resolution satellite images described by rational polynomials. *Photogrammetric Engineering & Remote Sensing*, 69(1): 59-68.

HU, Y. and TAO, C. V., 2002. Updating solutions of the rational function model using additional control information. *Photogrammetric Engineering & Remote Sensing*, 68(7): 715-723.

JACOBSEN, K., 2001. Automatic matching and generation of orthophotos from airborne and spaceborne line scanner images. *Joint Workshop of ISPRS Working group I/2, I/5 and IV/7 on High Resolution Mapping from space 2001*, Hannover. CD-ROM. 9 pages.

JACOBSEN, K., 2002. Mapping with IKONOS images. *Proceedings of the 22$_{nd}$ EARSeL Symposium*, Prague. EARSeL 48: 149–156.

KIM, T., 2000. A study on the epipolarity of linear pushbroom images. *Photogrammetric Engineering & Remote Sensing*, 66(8): 961-966.

LO, K. C. and MULDER, N. J., 1992. High precision DEM generation from SPOT stereo imagery by object space least squares matching. *International Archives of Photogrammetry and Remote Sensing*, 29(B3): 133-138.

MADANI, M., 1999. Real-time sensor-independent positioning by rational functions. *ISPRS Workshop on Direct versus Indirect Methods of Sensor Orientation*, Barcelona. 64-75.

MCGLONE, C., 1996. Sensor modeling in image registration. *Digital Photogrammetry*. American Society for Photogrammetry and Remote Sensing, Bethesda, Maryland. 247 pages: 115-123.

NGIS(NATIONAL GEOGRAPHIC INFORMATION SYSTEM) PRODUCT SPECIFICATION, 2002. http://www.moct.go.kr/mct_hpg/html/download/b12.hwp [Accessed: 1st October 2004].

NOGUCHI, M., FRASER, C. S., NAKAMURA, T., SHIMONO, T. and OKI, S., 2004. Accuracy assessment of QUICKBIRD stereo imagery *Photogrammetric Record*, 19(106): 128-137.

OGC(OPEN GIS CONSORTIUM), 1999. The OpenGIS abstract specification-topic 7: earth imagery. http://www.opengis.org/docs/99-107.pdf [Accessed: 1st October 2004].

OTTO, G. P., 1988. Rectification of SPOT data for stereo image matching. *International Archives of Photogrammetry and Remote Sensing*, 27(B3): 635-645.

QUICKBIRD PRODUCT GUIDE, 2003. http://www.digitalglobe.com/downloads/productguide.pdf [Accessed: 1st October 2004].

SOHN, H.-G., KIM, G.-H. and YOM, J.-H., 2004. Mathematical modeling of historical reconnaissance CORONA KH-4B imagery. *Photogrammetric Record*, 19(105): 51-66.

TAO, C. V., HU, Y., MERCER, J. B., SCHNICK, S. and ZHANG, Y., 2000. Image rectification using a generic sensor model – rational function model. *International Archives of Photogrammetry and Remote Sensing*, 33(B3): 874-881.

TAO, C. V. and HU, Y., 2001(a). The rational function model: a tool for processing high-resolution imagery. *Earth Observation Magazine*, 10(1): 13-16.

TAO, C. V. and HU, Y., 2001(b). A comprehensive study of the rational function model for photogrammetric processing. *Photogrammetric Engineering & Remote Sensing*, 67(12): 1347-1357.

TAO, C. V. and HU Y., 2001(c). Use of the rational function model for image rectification. *Canadian Journal of Remote Sensing*, 27(6): 593-602.

TAO, C. V. and HU, Y., 2002. 3D reconstruction methods based on the rational function model. *Photogrammetric Engineering & Remote Sensing*, 68(7): 705-714

YANG, X., 2000. Accuracy of rational function approximation in photogrammetry. *ASPRS Annual Convention*, Washington, D.C., CD-ROM. 10pages.

ZHANG, L., PATERAKI, M. and BALTSAVIAS, E., 2002. Matching of IKONOS stereo and multitemporal GEO images for DSM generation. *Map Asia 2002*, Bangkok, Malaysia, Poster paper.

ZHANG, Y., 1991. Matching in image/object dual spaces. *SPIE*, 1526: 195-202.

ZHANG, Z., DERICHE, R., FAUGERAS, O. and LUONG, Q.-T., 1995. A robust technique for matching two uncalibrated images through the recovery of the unknown epipolar geometry. *Artificial Intelligence Journal*, 78(1-2): 87-119.